Quantum projection noise: Population fluctuations in two-level systems

W. M. Itano, J. C. Bergquist, J. J. Bollinger, J. M. Gilligan, D. J. Heinzen,* F. L. Moore,*
M. G. Raizen,* and D. J. Wineland

Time and Frequency Division, National Institute of Standards and Technology, Boulder, Colorado 80303

(Received 9 December 1992)

Measurements of internal energy states of atomic ions confined in traps can be used to illustrate fundamental properties of quantum systems, because long relaxation times and observation times are available. In the experiments described here, a single ion or a few identical ions were prepared in well-defined superpositions of two internal energy eigenstates. The populations of the energy levels were then measured. For an individual ion, the outcome of the measurement is uncertain, unless the amplitude for one of the two eigenstates is zero, and is completely uncertain when the magnitudes of the two amplitudes are equal. In one experiment, a single ^{199}Hg$^+$ ion, confined in a linear rf trap, was prepared in various superpositions of two hyperfine states. In another experiment, groups of ^{9}Be$^+$ ions, ranging in size from about 5 to about 400 ions, were confined in a Penning trap and prepared in various superposition states. The measured population fluctuations were greater when the state amplitudes were equal than when one of the amplitudes was nearly zero, in agreement with the predictions of quantum mechanics. These fluctuations, which we call quantum projection noise, are the fundamental source of noise for population measurements with a fixed number of atoms. These fluctuations are of practical importance, since they contribute to the errors of atomic frequency standards.

I. INTRODUCTION

Quantum mechanics is not a deterministic theory, even though the time development of the quantum-state vector is governed by the Schrödinger equation, which *is* deterministic. That is, quantum mechanics does not, in general, predict the result of an experiment. Rather, it provides a prescription for predicting the *probability* of observing a given result. The relationship of the quantum-state vector to the physical system that it describes is central to the interpretation of quantum mechanics. There are at least two distinct interpretations of the quantum state [1].

According to the Copenhagen interpretation, the state vector provides a complete description of an individual system (a single atom, for example). This is not the only definition of the Copenhagen interpretation, but it is the one that we adopt here. According to this interpretation, the state vector of a system develops in time according to the Schrödinger equation until a measurement causes it to be projected into an eigenstate of the dynamical variable that is being measured. The assumption that the state vector "collapses" in this manner is considered unattractive by some, because of its *ad hoc* nature.

According to another interpretation, sometimes called the statistical-ensemble interpretation, the state vector is merely a mathematical construct which describes an ensemble of similarly prepared systems [2–4]. One common misconception is that this interpretation is not capable of describing an experiment on a single atom. In this case, the state vector describes a *conceptual ensemble* (a Gibbs ensemble) of similarly prepared atoms. The single atom in the experiment is a member of that ensemble. Experi-

mentally, an ensemble is generated by repeatedly preparing the state of the atom and then making a measurement. The state vector, in this interpretation, is analogous to a statistical distribution function of the kind that appears in classical statistical mechanics. The difference is that, in quantum mechanics, there is no underlying microscopic theory which can predict the behavior of a single system, even in principle. The statistical-ensemble interpretation has the virtue of avoiding the necessity of "reducing" or "collapsing" the state vector.

In spite of occasional claims to the contrary [5], it appears that the Copenhagen and statistical-ensemble interpretations do not differ in their predictions of experiments *when properly applied* [6]. In practice, either interpretation may motivate a particular calculation. For example, some problems in quantum optics have been solved by simulating the behavior of the wave function of a single atom, explicitly including the reduction of the wave function at random times [7–10]. Such methods follow naturally from the Copenhagen interpretation (which is not to say that the practitioners of these methods would necessarily advocate the Copenhagen interpretation as *opposed* to the statistical-ensemble interpretation). On the other hand, the conventional method of solving the density-matrix equations follows naturally from the statistical-ensemble interpretation. The results of averaging many wave-function simulations are the same as those of solving the density-matrix equations. The experiments described here can be interpreted within either framework.

Perhaps the simplest example of the indeterminism of quantum mechanics is the behavior of a two-level system prepared in a superposition $|\psi\rangle = c_A|A\rangle + c_B|B\rangle$ of the two states $|A\rangle$ and $|B\rangle$ and subjected to a measure-

ment. The measurement yields one indication or "pointer reading" for a system in $|A\rangle$ and another for a system in $|B\rangle$. Except when either c_A or c_B is zero, the outcome of the measurement cannot be predicted with certainty. Provided that the state vector is properly normalized ($|c_A|^2 + |c_B|^2 = 1$), $|c_A|^2 \equiv p_A$, and $|c_B|^2 \equiv p_B$ are the probabilities of finding the system in $|A\rangle$ or $|B\rangle$. The indeterminacy is present no matter how accurately the state has been prepared. It is an inherent feature of quantum mechanics. We will call this source of measurement fluctuations "quantum projection noise," since it can be interpreted as arising from the random projection of the state vector into one of the states compatible with the measurement process.

In some experiments we have a sample of N identical systems that are effectively independent. If we carry out the same kind of state preparation and measurement as that just described for a single system, then we should get the same result as by repeating the experiment N times. That is, the sum over all N atoms of the measured quantity should have the same mean and fluctuations as the sum of N independent measurements on one system.

The internal states of a set of N ions in an ion trap constitute a system of this type. The ions are well separated from each other by their mutual Coulomb repulsion, so, to a very good approximation, the state of one ion has no effect on that of another ion. If all of the ions are subjected to the same optical and radiofrequency fields, they can all be described by the same state vector for their internal degrees of freedom. In an ion trap, unlike an atomic beam, for example, we can repeatedly prepare and observe the *same* set of N atoms.

To illustrate the main ideas, we will first describe a simplified version of the experiment. The actual experiments, carried out with single $^{199}\text{Hg}^+$ ions in a linear rf trap and with numbers of $^9\text{Be}^+$ ions ranging from about 5 to 400 in a Penning trap, will be explained in detail in later sections.

Consider a single atom, or several identical atoms, with three energy levels $|A\rangle$, $|B\rangle$, and $|C\rangle$ (see Fig. 1). The
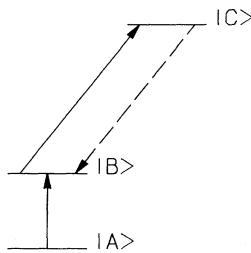

FIG. 1. A simplified energy-level diagram of an atom of the type used in the experiments. The atom or atoms are prepared in a superposition of $|A\rangle$ and $|B\rangle$ by a combination of laser optical pumping and rf excitation. The state is measured by applying laser radiation resonant with the $|B\rangle \rightarrow |C\rangle$ transition. If the atom is in $|A\rangle$, it does not absorb any photons from the laser beam and remains in $|A\rangle$. If the atom is in $|B\rangle$, the laser radiation drives it to $|C\rangle$. The atom then decays back to $|B\rangle$ and emits a photon. It can then be excited to $|C\rangle$ again.

lower two levels $|A\rangle$ and $|B\rangle$ are stable. They are separated by a radiofrequency photon energy. Level $|C\rangle$ decays, by emission of an optical photon, to $|B\rangle$ only. The state vector is prepared in a superposition of $|A\rangle$ and $|B\rangle$ by first preparing it in $|A\rangle$ and then applying an rf pulse near the $|A\rangle \rightarrow |B\rangle$ transition frequency. Any desired superposition of $|A\rangle$ and $|B\rangle$ can be obtained by controlling the frequency, amplitude, and duration of the rf pulse. The number of atoms in $|B\rangle$ is then measured. The measurement is made by applying a laser beam that is resonant with the transition from $|B\rangle$ to $|C\rangle$ and detecting the photons emitted in the decay from $|C\rangle$ to $|B\rangle$. If an atom is found in $|B\rangle$ when the laser pulse is applied, it is excited to $|C\rangle$. It quickly decays to $|B\rangle$ and emits a photon. It can then be excited back to $|C\rangle$ by the laser and emits another photon. Thus, an atom in $|B\rangle$ emits a series of many photons, while an atom in $|A\rangle$ emits none. The rate at which photons are emitted by the entire sample of atoms is proportional to the number of atoms in $|B\rangle$ when the laser beam is applied. If there is only one atom in the sample volume, the detection is particularly simple: If some photons are emitted, the atom was in $|B\rangle$; otherwise it was in $|A\rangle$. Quantum-amplification detection of this type, sometimes called electron shelving, was first proposed by Dehmelt [11] and, to the best of our knowledge, was first used by Wineland et al. [12].

In the preceding discussion, we assumed that each atom either emits a burst of photons or does not. According to the Copenhagen interpretation, the wave function of each atom is a superposition of $|A\rangle$ and $|B\rangle$ before the measurement and collapses to one state or the other when the detection laser beam is applied. According to the statistical-ensemble interpretation, the atom is found to be in $|A\rangle$ or $|B\rangle$ when the measurement is made, with probabilities p_A and p_B, respectively. There is no point in asking which state the atom was in just before the measurement, since this is not a question that can be answered by the experiment.

Quantum projection noise in the measured populations of states prepared in superpositions may be of some practical interest. This point was discussed previously, in the context of atomic frequency standards, by Wineland et al. in Appendix A of Ref. [13]. In some atomic frequency standards, such as cesium atomic beams, a signal which is proportional to the population of a particular quantum state is measured as a function of the frequency of an applied rf field. The signal is a maximum (or a minimum, depending on the detection method used) when the frequency matches the transition frequency ω_0 between two atomic states and decreases when the frequency increases or decreases from this value (see Fig. 2). The frequency ω of an oscillator is matched to the resonance frequency ω_0 by measuring the signal at two frequencies $\omega - \Delta\omega$ and $\omega + \Delta\omega$ and making a correction to ω by an amount proportional to the difference between the two signals. In the example shown in Fig. 2, the signal at $\omega + \Delta\omega$ is less than the signal at $\omega - \Delta\omega$, which indicates that ω must be decreased in order to match ω_0. If the noise is independent of the position on the resonance line shape, measurements at the points of maximum slope would give the greatest sensitivity for determining ω_0. However, the
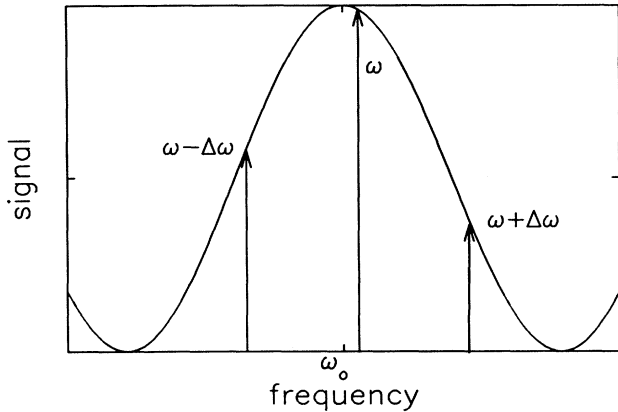
FIG. 2. A graph of the mean detected signal as a function of the frequency of the applied field for a resonance like that used in an atomic clock. The signal is proportional to the population of a particular energy level after the field has been applied. The maximum signal occurs at frequency ω_0. If the line shape is symmetric, ω_0 can be determined by measuring the signal at two different frequencies $\omega - \Delta\omega$ and $\omega + \Delta\omega$ and varying ω until the signal intensities are equal. The frequency ω determined in this way is an estimate of ω_0.

noise will in general vary with the signal level, due to quantum projection noise and also to other causes. Assume we have the extreme case where the only noise is quantum projection noise, where the maximum and the minima of the line shape correspond to pure energy eigenstates $|A\rangle$ and $|B\rangle$, and where the half-intensity points

correspond to equal superpositions of $|A\rangle$ and $|B\rangle$. In that case, it is not so obvious what the optimum value of $\Delta\omega$ should be. The noise goes to zero at the maxima and minima of the line shape, where the sensitivity to frequency deviations also goes to zero. The noise is the greatest at the half-intensity points, which, for a typical line shape, is where the frequency sensitivity is approximately the greatest. It will be shown later that the precision with which the line center can be determined is independent of $\Delta\omega$, if the line shape has a cosinusoidal form, often a good approximation when Ramsey's separated-oscillatory-field resonance method [14] is used.

II. THEORY

A. Single atom

Suppose a single system, such as a single atom, is prepared in a well-defined superposition of two stable or metastable states $|A\rangle$ and $|B\rangle$, which have energies $\hbar\omega_A$ and $\hbar\omega_B$. This could be done by preparing the atom in $|A\rangle$, by optical pumping, for example, and then applying a nearly resonant rf field of well-controlled frequency, amplitude, and duration. Suppose that the system is in $|A\rangle$ at time $t = 0$. We then apply an oscillatory perturbation V which has matrix elements:

$$\langle A|V|A\rangle = \langle B|V|B\rangle = 0, \tag{2.1}$$

$$\langle A|V|B\rangle = \langle B|V|A\rangle^* = \hbar b e^{i\omega t}. \tag{2.2}$$

The state at a later time $t > 0$ is [14]

$$|\psi(t)\rangle = c_A(t)|A\rangle + c_B(t)|B\rangle \tag{2.3}$$

$$= \left[i\frac{(\omega_0 - \omega)}{\Omega} \sin\left(\frac{\Omega t}{2}\right) + \cos\left(\frac{\Omega t}{2}\right) \right] \exp\left[\frac{i}{2}(\omega - \omega_A - \omega_B)t\right] |A\rangle$$

$$- i\frac{2b}{\Omega} \sin\left(\frac{\Omega t}{2}\right) \exp\left[-\frac{i}{2}(\omega - \omega_A - \omega_B)t\right] |B\rangle, \tag{2.4}$$

where

$$\omega_0 \equiv \omega_B - \omega_A, \tag{2.5}$$

$$\Omega \equiv \sqrt{(\omega_0 - \omega)^2 + (2b)^2}. \tag{2.6}$$

In deriving Eq. (2.4), we assumed that V does not induce transitions to states other than $|A\rangle$ and $|B\rangle$ and that spontaneous decay can be neglected. Also, all other perturbations, such as those due to collisions, are assumed to be negligible. For the levels studied experimentally in this work, which are hyperfine Zeeman sublevels of ground electronic states of atoms, spontaneous decay can be neglected. Such states decay primarily by magnetic dipole radiation. The rate for magnetic dipole decay from a higher sublevel $|e\rangle$ to a lower level $|g\rangle$ is

$$\gamma(e \rightarrow g) = \frac{4\omega_{eg}^3}{3\hbar c^3} |\langle e|\boldsymbol{\mu}|g\rangle|^2, \tag{2.7}$$

where $\hbar\omega_{eg}$ is the energy difference between $|e\rangle$ and $|g\rangle$ and $\boldsymbol{\mu}$ is the magnetic dipole operator. For typical values of the parameters for transitions between hyperfine-Zeeman sublevels, the mean lifetime for spontaneous decay is many years. For example, if $\omega_{eg} = 2\pi \times 30$ GHz and $|\langle e|\boldsymbol{\mu}|g\rangle| = \mu_B$, where μ_B is the Bohr magneton, then the decay rate given by Eq. (2.7) is 2.7×10^{-11} s^{-1}; that is, the lifetime is 1200 years.

In order to prepare a state with a given value of $p_B \equiv |c_B(t)|^2$, we can adjust b, ω, and the time t during which V is applied. For example, if $\omega = \omega_0$, then

$$p_B = \sin^2\left(\frac{\Omega t}{2}\right) = \sin^2(bt). \tag{2.8}$$

Any value of p_B from 0 to 1 can be obtained by adjusting the value of the product bt. Alternatively, it may be more convenient to vary ω, keeping b and t fixed at values so

that $bt = \pi$. (This is what is done in order to observe the resonance line shape, for example.) This induces a complete inversion ($p_B = 1$) at exact resonance ($\omega = \omega_0$). Any value of p_B down to 0 can be obtained by varying ω between ω_0 and $\omega_0 - 2\pi\sqrt{3}/t$ or between ω_0 and $\omega_0 + 2\pi\sqrt{3}/t$.

Ramsey's method of separated oscillatory fields [14] is another way of creating a given value of p_B. In this method, the perturbation is applied in two phase-coherent pulses of duration τ with a delay T between them. If the strength of the perturbation b is adjusted so that $b\tau = \pi/2$, then $p_B \equiv |c_B(T + 2\tau)|^2$ can be made to take any value between 0 and 1 by varying ω. If, in addition, $\tau \ll T$ and $|\omega - \omega_0|\tau \ll 1$, the probability p_B to be in $|B\rangle$ at time $T + 2\tau$ is

$$p_B \approx \tfrac{1}{2}\{1 + \cos[(\omega - \omega_0)T]\}. \tag{2.9}$$

An expression valid for arbitrary values of the parameters has been given by Ramsey [14].

It is useful to define a vector operator $\mathbf{r}$ on the subspace spanned by $|A\rangle$ and $|B\rangle$. The components of $\mathbf{r}$ are defined as

$$
\begin{aligned}
r_1 &\equiv \tfrac{1}{2}(|A\rangle\langle B| + |B\rangle\langle A|), \\
r_2 &\equiv \tfrac{i}{2}(|A\rangle\langle B| - |B\rangle\langle A|), \\
r_3 &\equiv \tfrac{1}{2}(|B\rangle\langle B| - |A\rangle\langle A|).
\end{aligned}
\tag{2.10}
$$

The operator $\mathbf{r}$ is equivalent to a spin-$\tfrac{1}{2}$ angular momentum operator, since it operates on a two-dimensional complex vector space and since the commutators satisfy the same algebra:

$$[r_i, r_j] = i\epsilon_{ijk}r_k, \tag{2.11}$$

where ϵ_{ijk} is the Levi-Civita symbol. For a general pure state of the form of Eq. (2.3), the expectation values of these operators are

$$
\begin{aligned}
\langle r_1 \rangle &= \tfrac{1}{2}(c_A^* c_B + c_B^* c_A) = \tfrac{1}{2}\sin\theta\,\cos\phi, \\
\langle r_2 \rangle &= \tfrac{i}{2}(c_A^* c_B - c_B^* c_A) = \tfrac{1}{2}\sin\theta\,\sin\phi, \\
\langle r_3 \rangle &= \tfrac{1}{2}(|c_B|^2 - |c_A|^2) = \tfrac{1}{2}\cos\theta,
\end{aligned}
\tag{2.12}
$$

where we have used the notation $\langle r_1 \rangle \equiv \langle \psi|r_1|\psi\rangle$, etc. The expectation values can be represented geometrically by a three-dimensional vector $\langle \mathbf{r} \rangle$ of length $\tfrac{1}{2}$. The spherical polar angles (θ, ϕ) define the orientation of $\langle \mathbf{r} \rangle$. As pointed out by Feynman, Vernon, and Hellwarth [15], this representation is sometimes useful because of the way in which the evolution of the quantum state can be visualized as a rotation of a vector. The quantities $\{2\langle r_1 \rangle, 2\langle r_2 \rangle, 2\langle r_3 \rangle\}$ are equivalent to the quantities $\{r_1, r_2, r_3\}$ defined by Feynman, Vernon, and Hellwarth. The reason for using the definition of $\mathbf{r}$ given by Eq. (2.10), rather than one differing by a factor of 2, is that $\mathbf{r}$ then corresponds precisely to a spin-$\tfrac{1}{2}$ angular momentum operator. The vector representation can be generalized to deal with mixed states (statistical ensembles of pure states), but that will not be necessary here. The third component of $\mathbf{r}$ is proportional to the internal energy operator. The

eigenstates of r_3 with eigenvalues $m = -\tfrac{1}{2}$ and $m = +\tfrac{1}{2}$ correspond to $|A\rangle$ and $|B\rangle$, respectively.

The variance of the measurement of the state ($|A\rangle$ or $|B\rangle$) of a single atom is particularly simple to calculate. We define a projection operator $P_B \equiv |B\rangle\langle B|$. The expectation value of P_B is $|c_B|^2 \equiv p_B$, the probability of a measurement finding the atom in $|B\rangle$. The variance of the measurement is

$$
\begin{aligned}
(\Delta P_B)^2 &\equiv \langle (P_B - \langle P_B \rangle)^2 \rangle \\
&= \langle P_B^2 - 2\langle P_B \rangle P_B + \langle P_B \rangle^2 \rangle \tag{2.13} \\
&= \langle P_B^2 \rangle - \langle P_B \rangle^2 = \langle P_B \rangle - \langle P_B \rangle^2 \tag{2.14} \\
&= \langle P_B \rangle(1 - \langle P_B \rangle) = p_B(1 - p_B). \tag{2.15}
\end{aligned}
$$

In Eq. (2.14), we have used the fact that

$$P_B^2 = (|B\rangle\langle B|)(|B\rangle\langle B|) = |B\rangle\langle B| = P_B. \tag{2.16}$$

Equation (2.15) shows that the uncertainty is zero when p_B is 0 or 1 and has its maximum value when $p_B = \tfrac{1}{2}$.

B. N atoms

If cooperative effects can be neglected over the time of the experiments, we may consider the atoms to be independent. For the systems used in the experiments, the decay rate of an individual atom is extremely small. It is possible for a suitably prepared collection of N atoms to exhibit a maximum spontaneous-decay rate per atom of about N times the usual rate given by Eq. (2.7), due to cooperative effects [16]. Even if the rate is enhanced by a factor of N, though, it can still be ignored for the small values of N that were used in these experiments.

One natural way to calculate the fluctuations of the measured populations is to consider the N atoms to be independent and to combine the probabilities according to the binomial distribution [17]. Let N_A and N_B be the numbers of atoms found to be in $|A\rangle$ and $|B\rangle$, respectively ($N_A + N_B = N$). Then, according to this model, the probability of measuring a given value of N_B is

$$P(N_B, N, p_B) = \frac{N!}{N_B!(N - N_B)!}(p_B)^{N_B}(1 - p_B)^{(N - N_B)}, \tag{2.17}$$

where $p_B \equiv |c_B|^2$ is the probability for a single atom to be in $|B\rangle$ and $(1 - p_B) = p_A \equiv |c_A|^2$ is the probability to be in $|A\rangle$. The variance of the binomial distribution is [17]

$$\sigma^2 = Np_B(1 - p_B). \tag{2.18}$$

The variance is zero when $p_B = 0$ or $p_B = 1$ and has its maximum value of $N/4$ when $p_B = \tfrac{1}{2}$. For $N = 1$, Eq. (2.18) agrees with Eq. (2.15). Figure 3 shows plots of probability distributions calculated from Eq. (2.17), for $N = 20$ and $p_B = 0, 0.1, \ldots, 1$.

In general, it would be better to use a formalism that treats the N atoms as a combined quantum system. This should give a correct description both when cooperative
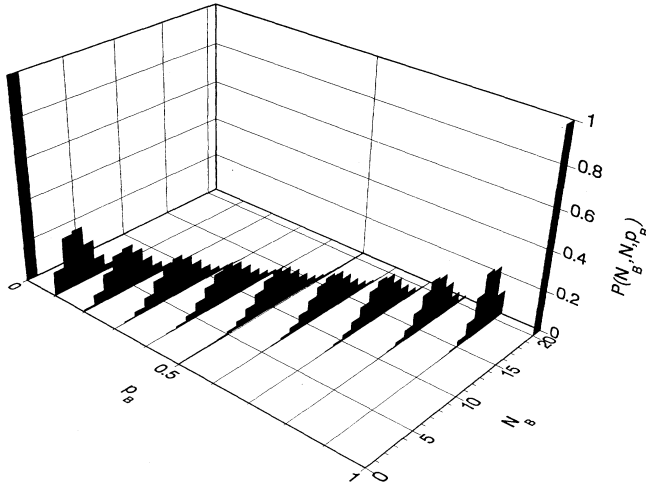
FIG. 3. A plot of the probability distributions of N_B, the number of atoms in $|B\rangle$, for $p_B = 0, 0.1, \ldots, 1$. The total number of atoms N is 20. As p_B increases from 0, the distribution broadens and reaches its maximum variance at $p_B = 0.5$. As p_B increases beyond 0.5 the distribution narrows, eventually becoming a spike at $N_B = 20$ for $p_B = 1$.

effects are important and when they are negligible. Each two-level atom can be described by a spin-$\frac{1}{2}$ operator $\mathbf{r}_i$, defined as in Eq. (2.10), where $i = 1, \ldots, N$ labels the atom. The eigenstates of r_{i_3} with eigenvalues $m_i = -\frac{1}{2}$ or $+\frac{1}{2}$ correspond, respectively, to the $|A\rangle$ and $|B\rangle$ states of the ith atom, which we denote by $|A_i\rangle$ and $|B_i\rangle$. One basis for the 2^N-dimensional Hilbert space of N atoms is provided by the direct-product states of the form

$$|m_1, m_2, \ldots, m_N\rangle \equiv \prod_{i=1}^{N} |m_i\rangle. \qquad (2.19)$$

A collective-angular-momentum operator for the N atoms can be defined by

$$\mathbf{R} \equiv \sum_{i=1}^{N} \mathbf{r}_i. \qquad (2.20)$$

It is implicitly assumed that each term in the summation is multiplied by the identity operators for all of the other atoms. Another basis for N atoms is given by states of the form $|g, R, M\rangle$, which are linear combinations of the product states defined by Eq. (2.19) [16]. Here, $R(R+1)$ is the eigenvalue of $\mathbf{R}^2$, M is the eigenvalue of R_3, and g is an index that may be required to provide a complete

set of labels. The eigenvalue M is related to the variables previously defined by

$$M = \tfrac{1}{2}(N_B - N_A), \qquad (2.21)$$

$$N_B = \tfrac{1}{2}N + M. \qquad (2.22)$$

Thus, fluctuations in M correspond directly to fluctuations in N_B, although M and N_B differ by a constant.

The state in which all of the atoms are in $|A\rangle$ has $R = \tfrac{1}{2}N$ and $M = -\tfrac{1}{2}N$ and is nondegenerate. This state is denoted by

$$|R = \tfrac{1}{2}N, M = -\tfrac{1}{2}N\rangle \equiv \prod_{i=1}^{N} |m_i = -\tfrac{1}{2}\rangle \equiv \prod_{i=1}^{N} |A_i\rangle.$$

$$(2.23)$$

We assume the atoms are far enough apart that they do not overlap spatially, so that symmetrization or antisymmetrization of the total wave function is unnecessary. Suppose that we apply the same perturbation to all of the atoms, so that the state of the ith atom goes to $c_A|A_i\rangle + c_B|B_i\rangle$ for each i. That is, the new state is

$$\prod_{i=1}^{N}(c_A|A_i\rangle + c_B|B_i\rangle). \qquad (2.24)$$

We can visualize this as a rotation of the collective state vector from the negative R_3 axis ($\theta = \pi$) to new values of θ and ϕ given in terms of c_A and c_B by Eq. (2.12). Equivalently, it can be described as a rotation of the coordinate system by $\pi - \theta$ about the original R_2 axis, followed by a rotation of $-\phi$ about the new R_3 axis. The properties of states of this kind were discussed by Arecchi *et al.* [18], who called them atomic coherent states. They also called them Bloch states, because they resemble the spin states studied in nuclear magnetic resonance. The new state given by Eq. (2.24) is a linear combination of the states $|R = \tfrac{1}{2}N, M\rangle$, for $M = -\tfrac{1}{2}N, -\tfrac{1}{2}N + 1, \ldots, \tfrac{1}{2}N$, since it is generated from Eq. (2.23) by a rotation. This state is

$$|R = \tfrac{1}{2}N, \theta, \phi\rangle = \sum_{M=-N/2}^{M=N/2} D_{M\ -N/2}^{(N/2)}(0, \pi - \theta, -\phi)$$

$$\times |R = \tfrac{1}{2}N, M\rangle, \qquad (2.25)$$

where $D_{M\ -N/2}^{(N/2)}$ is a matrix element of the rotation operator as defined in Eq. (4.1.10) of Ref. [19]. If the system is prepared in the state given by Eq. (2.25), the probability of measuring a given value of M is the absolute square of the coefficient of $|R = \tfrac{1}{2}N, M\rangle$, which is

$$P_{\text{Bloch}}(M, N, \theta) \equiv |D_{M\ -N/2}^{(N/2)}(0, \pi - \theta, -\phi)|^2 \qquad (2.26)$$

$$= \left[d_{M\ -N/2}^{(N/2)}(\pi - \theta)\right]^2 \qquad (2.27)$$

$$= \left[d_{M\ N/2}^{(N/2)}(\theta)\right]^2 \qquad (2.28)$$

$$= \frac{N!}{(\tfrac{1}{2}N + M)!(\tfrac{1}{2}N - M)!}\left(\cos\frac{\theta}{2}\right)^{N+2M}\left(\sin\frac{\theta}{2}\right)^{N-2M} \qquad (2.29)$$

$$= \frac{N!}{N_B!(N-N_B)!} \left(\cos^2 \frac{\theta}{2}\right)^{N_B} \left(\sin^2 \frac{\theta}{2}\right)^{(N-N_B)} \tag{2.30}$$

$$= \frac{N!}{N_B!(N-N_B)!} [\tfrac{1}{2}(1+\cos\theta)]^{N_B} [\tfrac{1}{2}(1-\cos\theta)]^{(N-N_B)} \tag{2.31}$$

$$= \frac{N!}{N_B!(N-N_B)!} (p_B)^{N_B} (1-p_B)^{(N-N_B)}. \tag{2.32}$$

The final result is the same as Eq. (2.17), which was obtained by another method. Arecchi $et\ al.$ obtained an equivalent result from the algebraic properties of the angular momentum operators, without explicitly making use of the rotation-operator matrix elements [18]. The quantity $d^{(N/2)}_{M-N/2}$ in Eq. (2.27) is defined in Eq. (4.1.12) of Ref. [19]. Equation (2.28) follows from Eq. (2.27) by making use of Eqs. (4.2.4)–(4.2.6) of Ref. [19]. The explicit form for $d^{(N/2)}_{M\,N/2}(\theta)$ given in Eq. (2.29) is from Eq. (4.1.27) of Ref. [19]. Equation (2.30) results from using Eq. (2.22) to express M in terms of N_B and N, and Eq. (2.31) follows by making use of trigonometric identities. The final expression [Eq. (2.32)] results from using Eq. (2.12) to express $\cos\theta$ in terms of $p_B \equiv |c_B|^2$.

The variance of the measured value of M can be calculated by the standard formula

$$(\Delta R_3)^2 = \langle R_3^2 \rangle - \langle R_3 \rangle^2. \tag{2.33}$$

For a state with the form of Eq. (2.24), in which the c_{A_i}'s and c_{B_i}'s are the same for all i, $\langle R_3 \rangle$ and $\langle R_3^2 \rangle$ can be easily be evaluated:

$$\langle R_3 \rangle = \frac{N}{2}(p_B - p_A), \tag{2.34}$$

and

$$\langle R_3^2 \rangle = \left\langle \left(\sum_{i=1}^{N} r_{i_3} \right)^2 \right\rangle \tag{2.35}$$

$$= \sum_{i=1}^{N} \sum_{j=1}^{N} \langle r_{i_3} r_{j_3} \rangle \tag{2.36}$$

$$= \sum_{i=1}^{N} \langle r_{i_3}^2 \rangle + \sum_{\substack{i,j \\ i \neq j}} \langle r_{i_3} r_{j_3} \rangle \tag{2.37}$$

$$= \frac{N}{4} + \frac{N(N-1)}{4}(p_B - p_A)^2. \tag{2.38}$$

In obtaining Eq. (2.38), we used the fact that the first sum in Eq. (2.37) contains N terms, all equal to

$$(c^*_{A_1}\langle A_1| + c^*_{B_1}\langle B_1|) r^2_{i_3} (c_{A_1}|A_1\rangle + c_{B_1}|B_1\rangle)$$

$$= \frac{|c_{A_1}|^2}{4} + \frac{|c_{B_1}|^2}{4} = \frac{1}{4}, \tag{2.39}$$

and the second sum contains $N(N-1)$ terms, all equal to

$$(c^*_{A_1}\langle A_1| + c^*_{B_1}\langle B_1|)(c^*_{A_2}\langle A_2| + c^*_{B_2}\langle B_2|) r_{i_3} r_{2_3}$$

$$\times (c_{A_1}|A_1\rangle + c_{B_1}|B_1\rangle)(c_{A_2}|A_2\rangle + c_{B_2}|B_2\rangle)$$

$$= \left(\frac{|c_{B_1}|^2}{2} - \frac{|c_{A_1}|^2}{2} \right) \left(\frac{|c_{B_2}|^2}{2} - \frac{|c_{A_2}|^2}{2} \right)$$

$$= \tfrac{1}{4}(p_B - p_A)^2. \tag{2.40}$$

Substituting the values of $\langle R_3 \rangle$ and $\langle R_3^2 \rangle$ from Eqs. (2.34) and (2.38) into Eq. (2.33), we obtain

$$(\Delta R_3)^2 = \frac{N}{4} + \frac{N(N-1)}{4}(p_B - p_A)^2 - \frac{N^2}{4}(p_B - p_A)^2$$

$$= \frac{N}{4}[1 - (p_B - p_A)^2]$$

$$= \frac{N}{4}\{1 - [p_B - (1 - p_B)]^2\}$$

$$= N p_B (1 - p_B). \tag{2.41}$$

This result agrees with Eq. (2.18), which was based on the properties of the binomial distribution. Equation (2.41) was derived for the special case of an uncorrelated N-atom system in which all of the atoms have the same state vector. For more general states, in which the state vectors of different atoms are correlated with each other, it may be possible for the variance to be either larger or smaller than this value [20–23].

The error of an atomic frequency standard depends on the ratio of the noise in the signal to the frequency derivative of the signal. Aside from an additive constant, the signal of an idealized frequency standard with N atoms is proportional to $\langle R_3 \rangle$. The quantum projection noise is proportional to $\sqrt{(\Delta R_3)^2}$. If the Ramsey method is used, so that p_B is given by Eq. (2.9), the ratio of the quantum projection noise to the frequency derivative is independent of the frequency ω at which the measurement is made:

$$\sqrt{(\Delta R_3)^2} = \tfrac{1}{2}\sqrt{N}\sin[(\omega - \omega_0)T], \tag{2.42}$$

$$\frac{\partial \langle R_3 \rangle}{\partial \omega} = \tfrac{1}{2}NT\sin[(\omega - \omega_0)T], \tag{2.43}$$

$$\frac{\sqrt{(\Delta R_3)^2}}{\dfrac{\partial \langle R_3 \rangle}{\partial \omega}} = \frac{1}{T\sqrt{N}}. \tag{2.44}$$

The error is proportional to $1/\sqrt{N}$, which is sometimes called the shot-noise limit. If noise from other sources is significant, the ratio is not constant, and it is best to

measure the signal near the points of maximum slope. If the Ramsey method is not used, the exact trade-off of Eq. (2.44) does not hold, but the situation is not greatly different.

A simple graphical representation of a Bloch state can be used to provide an estimate of $(\Delta R_3)^2$ which agrees qualitatively with the result of Eq. (2.41). We can represent the Bloch state $|R = \frac{1}{2}N, M = -\frac{1}{2}N\rangle \equiv |R = \frac{1}{2}N, \theta = \pi\rangle$ by the set of all vectors of length
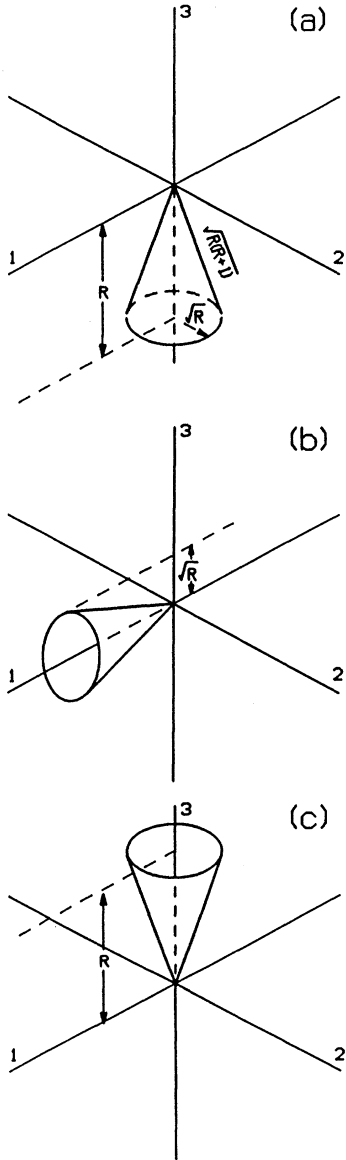

$\sqrt{R(R+1)}$ having their third (R_3) component equal to $-R$. This set forms a cone whose base has a radius equal to $\sqrt{R}$, as shown in Fig. 4(a). The fact that $(\Delta R_3)^2 = 0$ for this state is represented by the fact that all of the points on the circle surrounding the base of the cone have the same third component. The Bloch state $|R = \frac{1}{2}N, \theta = \frac{1}{2}\pi, \phi = 0\rangle$ is represented by Fig. 4(b). The points on the base of the cone have third components which vary over a range of $\pm\sqrt{R}$, while the rms deviation is approximately $\sqrt{R/2}$. Thus, we obtain the estimate $(\Delta R_3)^2 \approx R/2$. For a Bloch state with an arbitrary value of θ, we can use the same method to make the estimate

$$(\Delta R_3)^2 \approx \frac{R}{2}\sin^2\theta = Np_B(1 - p_B). \qquad (2.45)$$

This agrees with the actual value, which is given by Eq. (2.41). The Bloch state $|R = \frac{1}{2}N, \theta = 0\rangle$ is represented by Fig. 4(c). For this state, $(\Delta R_3)^2 = 0$.

III. SINGLE-ATOM EXPERIMENT

Quantum-state preparation and detection experiments were carried out with ^{199}Hg$^+$ ions confined in a linear rf trap. Detailed observations were made of single ions, although some experiments were also carried out with several simultaneously trapped ions.

A. ^{199}Hg$^+$ energy levels

Figure 5 shows the energy levels of ^{199}Hg$^+$ which were important for the experiments. The ground electronic state has the configuration $5d^{10}6s\,^2S_{1/2}$. The first electric dipole transition, at 194 nm, is to the $5d^{10}6p\,^2P_{1/2}$ state. The metastable $5d^96s^2\,^2D_{3/2}$ and $5d^96s^2\,^2D_{5/2}$ states (not shown in Fig. 5) lie below the $^2P_{1/2}$ state. The ^{199}Hg nucleus has spin $\frac{1}{2}$, so both the $^2S_{1/2}$ and the $^2P_{1/2}$ states are split by hyperfine interactions into states with total angular momentum $F = 0$ and $F = 1$. For both the $^2S_{1/2}$ and $^2P_{1/2}$ states, the $F = 1$ hyperfine state is higher in energy than the $F = 0$ hyperfine state. The $^2S_{1/2}$ hyperfine split-
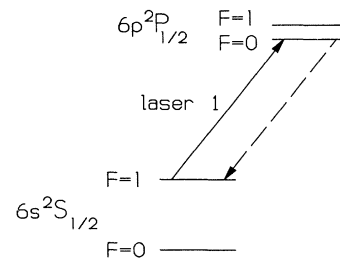
FIG. 4. Graphical representations of Bloch states (a) $|R = \frac{1}{2}N, M = -\frac{1}{2}N\rangle \equiv |R = \frac{1}{2}N, \theta = \pi\rangle$, (b) $|R = \frac{1}{2}N, \theta = \frac{\pi}{2}, \phi = 0\rangle$, and (c) $|R = \frac{1}{2}N, \theta = 0\rangle$. The uncertainty in the number of atoms in $|B\rangle$ (or $|A\rangle$) is represented by the spread in the third (R_3) component for the points on the circle surrounding the base of the cone. The uncertainty goes to zero for (a) and (c) and has its largest value for (b).

FIG. 5. Energy levels of ^{199}Hg$^+$. The transition between the $^2S_{1/2}$ and $^2P_{1/2}$ states is at 194 nm. The hyperfine splittings in the $^2S_{1/2}$ and $^2P_{1/2}$ states are 40.5 and 6.9 GHz, respectively. The $^2S_{1/2}$ $(F = 1)$ state is detected by exciting the $^2S_{1/2}$ $(F = 1) \rightarrow {}^2P_{1/2}$ $(F = 0)$ transition with laser 1.

ting has been measured by microwave resonance methods to be 40.507 347 996 9(3) GHz [24]. The $^2P_{1/2}$ hyperfine splitting has been measured by Fabry-Pérot interferometry to be 6.955(90) GHz [25]. The natural linewidth of the $^2P_{1/2}$ state is about 70 MHz [26,27].

B. Apparatus

The ^{199}Hg$^+$ ions were confined in a linear rf trap that consisted of four parallel cylindrical electrodes of radius 0.794 mm arranged symmetrically around a central axis [28]. The distance from the central axis to the inner surface of each electrode was 0.769 mm. The rf potentials on any two adjacent electrodes were 180° out of phase. The amplitude of the rf potential difference between two adjacent electrodes was about 500 V, and its frequency was 12.7 MHz. The electric fields produced by these electrodes created a force which pushed the ions to the central axis. The electrodes were divided into sections, to which static electric potentials of 1 V or less were applied to keep the ions from escaping along the axis.

Ions were produced by electron-impact ionization of neutral atoms inside the trap volume. A sample of ^{199}Hg of isotopic purity 91% was used. Typically, the pressure was about 10^{-7} Pa (1 Pa $\approx$ 7.5 mTorr), except when the ions were being created, when it was raised to a higher level. The ions were confined to a region of a few hundred micrometers extent around the center of the trap. After being laser cooled, an individual ion was localized in position to about 1 μm or less.

Narrow-band cw radiation at 194 nm was required for laser cooling and optical detection of the ^{199}Hg$^+$ ions. This was generated by a combination of second-harmonic generation and sum-frequency mixing, starting with cw lasers [29]. About 5 μW of 194-nm radiation were available. In order to laser cool and continuously observe the ions, 194-nm radiation near both the $^2S_{1/2}(F = 1) \rightarrow$ $^2P_{1/2}(F = 0)$ and the $^2S_{1/2}(F = 0) \rightarrow$ $^2P_{1/2}(F = 1)$ transition wavelengths was required [28]. We call these two sources laser 1 and laser 2. Otherwise, with only laser 1 or laser 2 on, the ions were optically pumped to a hyperfine state which could not absorb the 194-nm radiation. Also, in order to prevent trapping of the ions in Zeeman sublevels of the $^2S_{1/2}(F = 1)$ state, we had to apply a magnetic field of approximately 5×10^{-4} T at an angle of approximately 45° with respect to the electric field vector of the radiation from laser 1 (see Appendix). The magnitude and orientation of the magnetic field were controlled by several pairs of Helmholtz coils. The 194-nm beams were directed through the trap at an angle of 9° with respect to the trap axis, so that both the axial and radial degrees of freedom were laser cooled. For this geometry, the theoretical Doppler cooling limit was 1.1 mK for the axial motion and 24 mK for the radial motion [30].

Some of the 194-nm radiation emitted by the ions perpendicular to the trap axis was focused by a multi-element lens onto a two-dimensional imaging photon-counting tube. The probability of a photon emitted by an ion being detected was about 10^{-4}. Individual ions could

be resolved with this apparatus. Some images showing several clearly resolved ions have been published previously [28]. The electronics could be adjusted so that the photons from any rectangular region of the image, for example, a region including only one ion, could be counted separately. To a good approximation, the ions in the trap do not interact and are independent.

A stable source of 40.5-GHz radiation was required for exciting the $^2S_{1/2}(F = 0) \rightarrow (F = 1)$ hyperfine transition. The output of a 10.125-GHz frequency synthesizer was amplified and then frequency multiplied by four. The output of the frequency multiplier was directed at the ions with a horn antenna.

The data from the photon-counting tube were recorded by a computer. The computer also controlled the light shutters, a microwave switch, the frequency of the microwave frequency synthesizer, and the magnitude and orientation of the magnetic field.

C. State preparation and detection

Optical pumping can be used to prepare the ions in either the $(F = 1)$ or the $(F = 0)$ hyperfine level of the $^2S_{1/2}$ ground state. In order to prepare them in the $(F = 1)$ state, both laser 1 and laser 2 are left on. If an ion in the ground $(F = 1)$ state is excited to the $^2P_{1/2}(F = 0)$ state, it is forbidden by electric dipole selection rules from decaying to the ground $(F = 0)$ state, so it must return to the $(F = 1)$ state. There is a weak transition rate from the ground $(F = 1)$ state to the ground $(F = 0)$ state, via the $^2P_{1/2}(F = 1)$ state. This rate is approximately 3×10^{-5} times the rate of leaving the ground $(F = 1)$ state and returning to the same state, via the $^2P_{1/2}(F = 0)$ state, since laser 1 is far from resonance with the $^2S_{1/2}(F = 1) \rightarrow ^2P_{1/2}(F = 1)$ transition. If an ion does make a transition to the ground $(F = 0)$ state, laser 2 quickly drives it back to the $^2P_{1/2}(F = 1)$ state, which decays, with probability $\frac{2}{3}$, to the ground $(F = 1)$ state. If laser 1 and laser 2 are both blocked at the same time, the ion will be in the ground $(F = 1)$ state with high probability, after a few multiples of the $^2P_{1/2}$ state lifetime (2.3 ns). This method does not select out a particular M_F Zeeman sublevel of the ground $(F = 1)$ state. If desired, a single M_F state could be selected by switching the polarization of laser 1 (to right or left circular polarization with propagation along the magnetic field for $M_F = \pm 1$ or linear polarization perpendicular to the magnetic field for $M_F = 0$). However, this was not done in this work.

An ion can be prepared in the $^2S_{1/2}(F = 0)$ hyperfine level by blocking laser 2 while leaving laser 1 unblocked. For a typical intensity of laser 1, the ion is pumped to the ground $(F = 0)$ state in about 10 ms. In contrast to the previous method, the ion is prepared in a single M_F state. Laser 1 can also pump an ion from the ground $(F = 0)$ state to the ground $(F = 1)$ state. However, the rate for $(F = 0) \rightarrow (F = 1)$ is less than that for $(F = 1) \rightarrow (F = 0)$, mainly because laser 1 is farther from resonance for this process. In the steady state, the probability of being in the $(F = 0)$ state is about 94% (see Appendix). A

possible way to improve the state selection, for a single ion, is to observe the 194-nm photons emitted and to block laser 1 when the fluorescence drops to zero.

There is a probability of about 10^{-7} that an ion in the $^2P_{1/2}$ state will decay to the $^2D_{3/2}$ metastable state rather than to the $^2S_{1/2}$ state [27]. The $^2D_{3/2}$ state has a lifetime of 9.2 ms and decays, with about equal probability, to the $^2S_{1/2}$ state or to the metastable $^2D_{5/2}$ state, which has a lifetime of 86 ms [27,31]. This process is a potential problem for the state-selection methods, since the metastable states decay randomly to both ground hyperfine states. The effect was kept small by reducing the intensity of laser 1 so that the transition rate to the $^2D_{3/2}$ state was less than about 1 s^{-1}.

After the ion was prepared in the ground ($F = 0$) state, any desired superposition with the ground ($F = 1, M_F = 0$) state could be created by applying rf fields of well-controlled frequency, amplitude, and duration. These two states were used, because the magnetic shift of the transition frequency is quadratic, rather than linear, in the field. Thus, the transition frequency was stable enough to create the superposition states consistently.

State detection was carried out by counting the 194-nm photons emitted by the ions for a period, typically 15 ms, with laser 1 unblocked and laser 2 blocked. The mean number of photons detected was proportional to the number of ions in the ($F = 1$) state. However, the number is subject to statistical fluctuations, since the detection is essentially a Poissonian process. Also, laser intensity fluctuations lead to fluctuations in the overall counting rate.

Quantitative studies were made with only a single ion. In this case, the ion was presumed to be in the ($F = 1$) state if the number of photons detected was greater than a given threshold value and in the ($F = 0$) state if it was not. This threshold was set empirically, and was usually either 0 or 1. There was some possibility of error with this detection method. Dark counts from the phototube or photons scattered from some surface and then detected could lead to a false ($F = 1$) signal. Also, since the mean number of photons detected from an ($F = 1$) ion was small (about 5 in 15 ms), it was possible that not enough of them would be observed, thus leading to a false ($F = 0$) signal. If the detection efficiency could be improved, both of these problems could be reduced by using a higher threshold number of photons to distinguish between ($F = 1$) and ($F = 0$).

D. Results

The ability to prepare an ion in either the ($F = 0$) or ($F = 1$) ground hyperfine state is shown in Fig. 6. Each vertical line denotes the detection of a single photon at a particular time. The detection electronics were adjusted so that photons from only a single ion were detected. Before recording the data shown in Fig. 6(a), the ion was prepared in the ground ($F = 1$) state by leaving both laser 1 and laser 2 unblocked for about 0.1 s and then blocking them both. After a short delay, laser 1 was unblocked, and for 0.1 s, the photons were counted.
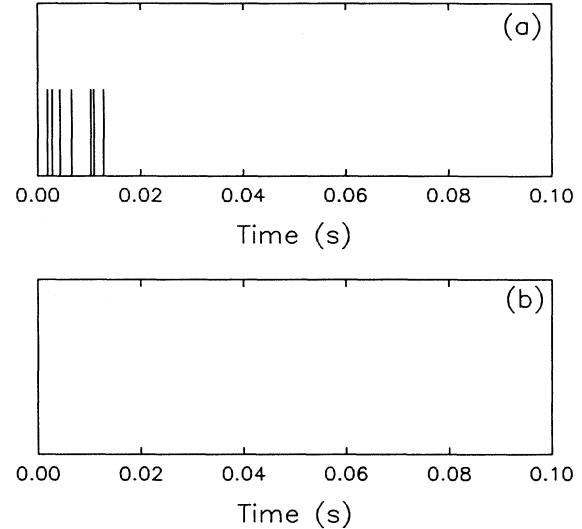

FIG. 6. Typical record of the detected photons from a single $^{199}Hg^+$ ion prepared in the ground (a) ($F = 1$) state and (b) ($F = 0$) state. The horizontal axis represents the time after laser 1, the detection laser, is unblocked. Each vertical line represents the detection of a single photon. In (a), eight photons were detected (two photons were too close in time to resolve on the graph). In (b), no photons were detected.

Their detection times were recorded with a resolution of 100 μs. In the example shown in Fig. 6(a), eight photons were recorded, but two of them were too nearly simultaneous to be resolved on the graph. Before recording the data shown in Fig. 6(b), the ion was prepared in the ground ($F = 0$) state by leaving laser 1 unblocked and laser 2 blocked for 0.05 s. Laser 1 was then blocked. After a short delay, laser 1 was unblocked again, and the computer was set to record photons, as for Fig. 6(a). None was recorded, so, with high probability, the ion was in the ($F = 0$) state.

Figure 7 shows the results of 100 successive single-ion state preparation and detection cycles of the type shown in Fig. 6. Preparation of the ($F = 1$) state [Fig. 7(a)] was alternated with that of the ($F = 0$) state [Fig. 7(b)], so that slow drifts in parameters such as the laser intensity would affect both plots in the same way. Each point represents the mean photon-count rate during a given 0.5-ms period after laser 1 was unblocked. The data from the first 1.5 ms, which was the time required for the light shutter to open fully, are not shown. The solid curve in Fig. 7(a) is a least-squares fit of the data to a decreasing exponential plus a constant base line. The fitted time constant of the exponential is 8.66 ±0.41 ms. The fitted amplitude of the exponential is 769 ± 22 counts/s. The fitted base line is 47.3 ± 4.3 counts/s. The solid line in Fig. 7(b) corresponds to 47.3 counts/s, the base line determined from Fig. 7(a). This value does not differ significantly from the mean of all of the points in Fig. 7(b), which is 50.05 counts/s. The background count rate due to all sources other than photons emitted by the ion was measured by detuning laser 1 far from resonance. This
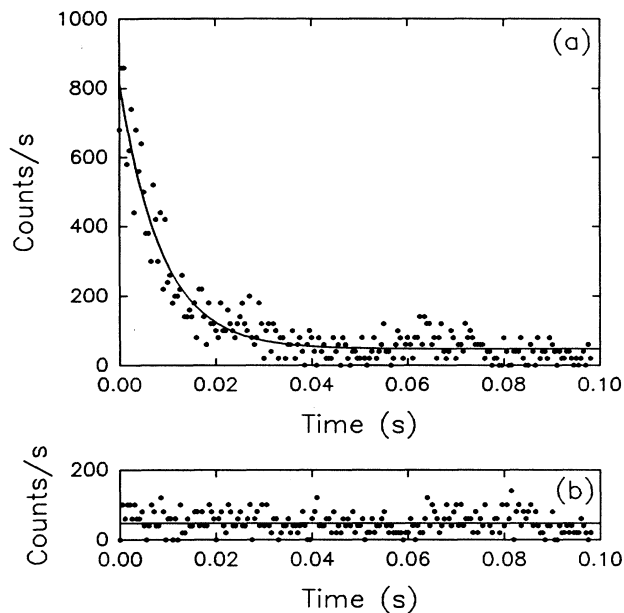
FIG. 7. Plot of the mean photon count rate as a function of the time after unblocking laser 1 for (a) a single ion prepared in the $(F = 1)$ state and (b) the same ion prepared in the $(F = 0)$ state. These plots were generated from 100 measurements like those in Fig. 6. The solid curve in (a) is a least-squares fit of the data to a decreasing exponential plus a baseline. The solid line in (b) is the base line determined from (a). The origin of the time axis is 1.5 ms after the laser 1 shutter is activated. After 1.5 ms this shutter is fully open.

rate was 4 ± 2 counts/s, so the actual base line for light scattered from the ion was 43 ± 5 counts/s. The ratio of the base line to the sum of the base line and the amplitude of the exponential is 0.053 ± 0.006. This represents the steady-state probability that an ion is in the ground $(F = 1)$ state when laser 1 alone is applied. This compares well with a calculated value of approximately 0.06 (see Appendix).

The Rabi resonance line shape shown in Fig. 8 was measured by repeatedly preparing the $(F = 0)$ state, applying a microwave pulse at a given frequency, and determining whether the ion was in $(F = 0)$ or $(F = 1)$. At each frequency, 19 measurements were made, and the results were averaged $[(F = 0)$ corresponding to 0 and $(F = 1)$ to 1]. For this run, the sequence of operations for each measurement was as follows.

(1) Both laser 1 and laser 2 were left on for 200 ms to laser cool the ion. The magnetic field was set to about 5×10^{-4} T to avoid optical pumping.

(2) The fluorescence from the ion was measured for 5 ms. This step was repeated if the number of photons counted was 50 or less. This was done to avoid proceeding while the ion was trapped in one of the metastable D states.

(3) Laser 2 was blocked to allow the ion to be pumped to the ground $(F = 0)$ state. The fluorescence was measured for 10 ms. If any photons were detected during this

period, another 10-ms measurement was made. This was to ensure that the ion was in the ground $(F = 0)$ state before proceeding.

(4) Laser 1 was blocked, and the magnetic field was decreased to approximately 5×10^{-5} T in order to reduce the effect of magnetic field fluctuations on the resonance frequency. A 30-ms rf pulse near the 40.5-GHz resonance was applied. The magnetic field was then increased to its previous value.

(5) Laser 1 was unblocked, and the fluorescence was measured for 15 ms. If 0 or 1 photons were detected, the ion was assumed to be in $(F = 0)$. If more photons were detected, it was assumed to be in $(F = 1)$.

The dashed line is a theoretical Rabi line shape for optimum power and a 30-ms rf pulse duration, calculated from Eq. (2.4). The deviation between the data and the calculation is most obvious at the minima of the line shape. The deviations result from the combined effects of imperfect $(F = 0)$ state preparation and imperfect state detection. The combination of these effects results in a signal that goes from about 0.1 to 0.95 instead of from 0 to 1. The frequency instability of the microwave source is known, from separate measurements, to be small enough as to have a negligible effect on the line shape [28].

We can also compute the variance of the signal at various positions on the resonance curve. At the point corresponding to the maximum signal, it is 0.053. At the two points corresponding approximately to the half-maximum points, it is 0.26. At the two points corresponding to the minimum signal on both sides of the resonance, it is 0.051.

We have published a microwave resonance curve in which the total fluorescence from several ions was measured [28]. Such a signal is more sensitive to noise from the intensity fluctuations of the 194-nm sources, background scattered light, and other sources. In order to reduce this noise, it should be possible to count the photons from each ion separately, in order to clearly discriminate between ions in the ground $(F = 0)$ and $(F = 1)$ states,
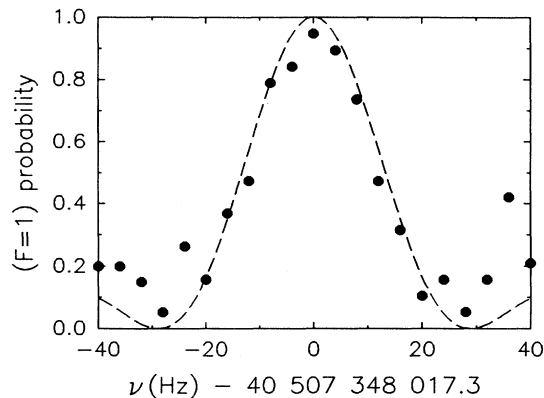
FIG. 8. Microwave resonance of a single ion. Each dot represents the average of 19 measurements. The curve is a calculated Rabi line shape. The calculation does not take into account the imperfect state preparation.
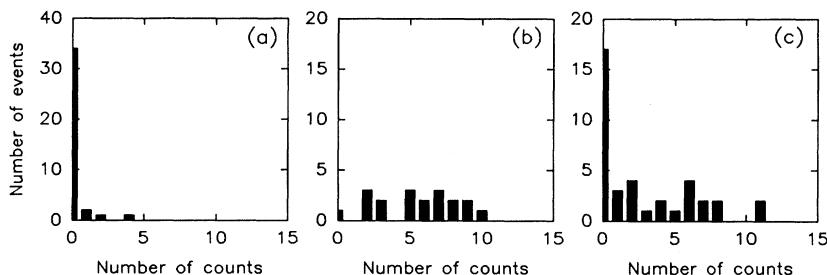
FIG. 9. Photon count distributions for a single ^{199}Hg$^+$ ion prepared in (a) the ($F=0$, $M_F=0$) state, (b) the ($F=1$, $M_F=0$) state, and (c) an equal superposition of these two states. The bars represent the number of cases in which a given number of fluorescence photons was detected when the detection laser was applied. The number of measurements was 38 for (a), 19 for (b), and 38 for (c).

as was done here with a single ion.

Figure 9 shows the distributions of the numbers of photons detected at various points on the resonance curve of Fig. 8. Figure 9(a) shows the distribution at the points corresponding to the minima on both sides of the resonance. In most cases, no photons were observed. However, in a few cases one or more photons were observed, presumably due to a combination of background scattered light and imperfect state preparation. Figure 9(b) shows the distribution at the maximum of the resonance. There is a broad distribution of numbers of photons detected, with a mean of about 5.5. In one measurement, no photons were measured. This may have been due to imperfect state preparation or to the possibility that no photons were detected, even though some were emitted. Figure 9(c) shows the distribution at the two half-maximum points on the resonance. The distribution is a superposition of those at the maximum and the minima. This bimodal distribution is the signature of the quantum projection noise for the single-atom case. That is, for a superposition state with equal amplitudes of the two components, the measurement finds the ion randomly in one state or the other.

IV. *N*-ATOM EXPERIMENT

N-atom quantum-state preparation and detection experiments were carried out with ^{9}Be$^+$ ions in a Penning trap. The Penning trap was used, rather than the rf trap, because the number of atoms that could be stably trapped could be varied from a few to several thousand. However, loading and detecting single ions was difficult with this apparatus.

A. ^{9}Be$^+$ energy levels

Figure 10 shows the energy levels of ^{9}Be$^+$ which were important for the experiments. The ground electronic state has the configuration $2s\,^2S_{1/2}$. The ^{9}Be nucleus has spin $\frac{3}{2}$, so the ground state has eight hyperfine Zeeman sublevels. In a high magnetic field, as is present in the Penning trap, the energy eigenstates are approximate eigenstates of I_z and J_z, the z components of the nuclear and electronic angular momenta. The static magnetic-field direction defines the z axis. These eigenstates will be referred to by their main components in the $|M_I, M_J\rangle$ basis. For brevity, they will also be referred to by num-

bers 1–8, as shown in Fig. 10, which correspond, in order of decreasing energy, to $|-\frac{3}{2}, +\frac{1}{2}\rangle$, $|-\frac{1}{2}, +\frac{1}{2}\rangle$, $|+\frac{1}{2}, +\frac{1}{2}\rangle$, $|+\frac{3}{2}, +\frac{1}{2}\rangle$, $|+\frac{3}{2}, -\frac{1}{2}\rangle$, $|+\frac{1}{2}, -\frac{1}{2}\rangle$, $|-\frac{1}{2}, -\frac{1}{2}\rangle$, and $|-\frac{3}{2}, -\frac{1}{2}\rangle$. The 313-nm transition to the $2p\,^2P_{3/2}$ electronic state was used for state selection and detection.

B. Apparatus

The experimental apparatus and techniques have been described previously [32–35]. The Penning trap was made of cylindrical electrodes, to which static electric potentials were applied. It was inserted into the bore of a superconducting solenoid magnet, which generated a uniform magnetic field B_0 of approximately 0.82 T. The combination of the electrostatic potentials and uniform magnetic field trapped the ions in three dimensions. The pressure in the trap was approximately 10^{-8} Pa. The ions were created by electron-impact ionization of neutral atoms.

The state preparation experiments required that the 313-nm light be blocked for some periods in order to avoid
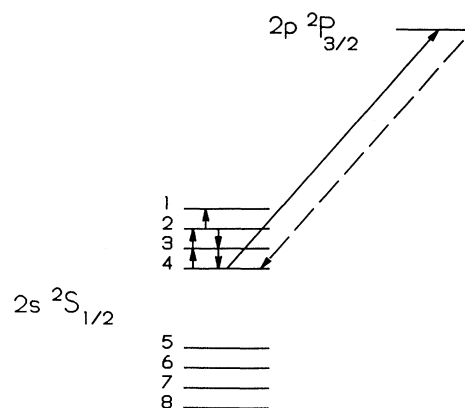

FIG. 10. Level diagram for ^{9}Be$^+$. The ground-state Zeeman hyperfine states are labeled by numbers 1–8. Their quantum numbers are given in the text. Laser radiation at 313 nm optically pumps most of the ions into state 4. These atoms are then transferred to state 3 and then to state 2 by rf π pulses. Other rf pulses then create a superposition of states 1 and 2. Atoms which remain in state 2 are transferred back to state 4. The laser radiation is applied again, and the number of atoms in state 4 is determined from the fluorescence intensity in the first second after the laser radiation is reapplied.

perturbations of the energy levels. In order to keep the ^{9}Be$^+$ ion plasma from heating and increasing its spatial extent when the 313-nm light was not available for laser cooling, approximately 1000 ^{26}Mg$^+$ ions were trapped and laser cooled at the same time. This cooled the ^{9}Be$^+$ ions by long-range Coulomb collisions [36]. The 280-nm $3s\,^2S_{1/2} \rightarrow 3p\,^2P_{3/2}$ transition was used for laser cooling the ^{26}Mg$^+$ ions.

The 313-nm and 280-nm beams required for state selection and detection of the ^{9}Be$^+$ ions and for laser cooling the ^{26}Mg$^+$ were generated by frequency doubling the outputs of cw dye lasers in nonlinear crystals. Fluorescence from the ions was focused by a multielement lens onto the photocathode of an imaging photon-counting tube. The overall detection efficiency was approximately 2×10^{-4}. To generate the rf magnetic fields required for the state preparation and detection, the amplified output of a frequency synthesizer was coupled into a wire loop antenna. The light shutters, rf switches, and frequency synthesizer were controlled by a computer, which also recorded the photon counts.

C. Ion-number measurement

In the ^{199}Hg$^+$ experiments, the number of ions could be determined directly from the image. This could not be done for the ^{9}Be$^+$ ions in the Penning trap, since they rotate rapidly around the z axis. Therefore, the number was determined indirectly. Calculations based on a charged fluid model relate the density of the ion plasma to its shape, for given external fields [36–38]. The shapes and sizes of the nonneutral, ion plasmas were determined by moving the laser beam and observing the imaged fluorescence. The product of the density and volume yielded the number of ions with an uncertainty estimated to be about 30%.

D. State preparation and detection

In the ^{9}Be$^+$ experiments, coherent superpositions of two internal states (states 1 and 2) were created and then subjected to measurements. These states were chosen because, for a value of B_0 near 0.8194 T, the first derivative of the transition frequency with respect to B_0 goes to zero. The resulting insensitivity to magnetic-field fluctuations makes it easier to generate coherent superposition states reproducibly.

The state preparation began by subjecting the ions to 313-nm radiation, polarized perpendicular to the magnetic field, for approximately 15 s. The frequency of the 313-nm radiation was slightly below the $2s\,^2S_{1/2}$ ($M_I = +\frac{3}{2}, M_J = +\frac{1}{2}$) $\rightarrow 2p\,^2P_{3/2}$ ($M_J = +\frac{3}{2}, M_I = +\frac{3}{2}$) transition frequency. This is a cycling transition, since electric dipole selection rules require that the ion return to the ground-state sublevel that it started from. Spontaneous Raman transitions induced by the 313-nm radiation established a steady state in which approximately $\frac{16}{17}$ of the ions were in state 4 and the remaining $\frac{1}{17}$ were in state

5. This optical pumping has been discussed previously [12,39] and studied experimentally [40]. There are fluctuations about these average values, since any given ion is continually making transitions between states. The ions could have been completely optically pumped into state 4 by circularly polarized light propagating along the z axis, but this was not convenient experimentally.

The 313-nm beam was blocked to stop the optical pumping and to prevent perturbations to the ^{9}Be$^+$ energy levels. Next, the ions in state 4 were transferred to state 3 and then to state 2 by 0.2 s resonant rf pulses. These were π pulses; that is, the products of the rf magnetic fields and the pulse durations were adjusted so that $bt = \pi$ in Eq. (2.8). The frequencies were 320 712 280 Hz for the (4 $\rightarrow$ 3) transition and 311 493 688 Hz for the (3 $\rightarrow$ 2) transition. The Ramsey method was then used to create various superpositions of states 1 and 2. The two Ramsey rf pulses were 0.5 s long and were separated by 5 s; the frequency was 303 016 377.265 Hz.

Then a measurement was made of the number of ions in state 2. First, the ions in state 2 were transferred to state 3 and then to state 4 by applying the π pulses in the opposite order. Then the 313-nm beam was unblocked, and the fluorescence photons were counted for 1 s.

The ions which were left in state 5 at the time that the 313-nm beam was blocked (about $\frac{1}{17}$ of the total number) contributed to the fluorescence signal. This is so, because the time constant for exchanging population between states 4 and 5 by spontaneous Raman transitions was about 0.1 s, which was much less than the 1-s observation time. The time constant for ions in state 1 to be optically pumped to states 4 and 5 was approximately 10 s. Therefore, the number of ions pumped from state 1 back to states 4 and 5 could be neglected.

E. Results

Ion plasmas containing numbers of ^{9}Be$^+$ ions ranging from a few to a few hundred were studied. Figures 11(a)–11(d) show the results from plasmas containing approximately 5, 21, 72, and 385 ions. The rf power for the (2 $\rightarrow$ 1) Ramsey resonance was adjusted so as to give a minimum fluorescence signal at the line center. Measurements were made at rf frequencies corresponding to the transition maximum (minimum fluorescence), the first upper and lower transition minima (maximum fluorescence), and the points halfway between the transition maximum and the upper and lower transition minima. The measured signal is the number of photons detected in the first second after the laser is unblocked. This is

$$S = B + K(N_4 + N_5), \qquad (4.1)$$

where B is the background signal, N_4 and N_5 are the numbers of ions in states 4 and 5, and K is a constant which must be calibrated for a given set of conditions. At the line center, the signal is $B + (KN/17)$, where N is the total number of ^{9}Be$^+$ ions, while at the points of maximum fluorescence, it is $B + KN$. For the $N = 5, 21,$ 72, and 385 data shown in Figs. 11(a)–11(d), $K = 87.3,$
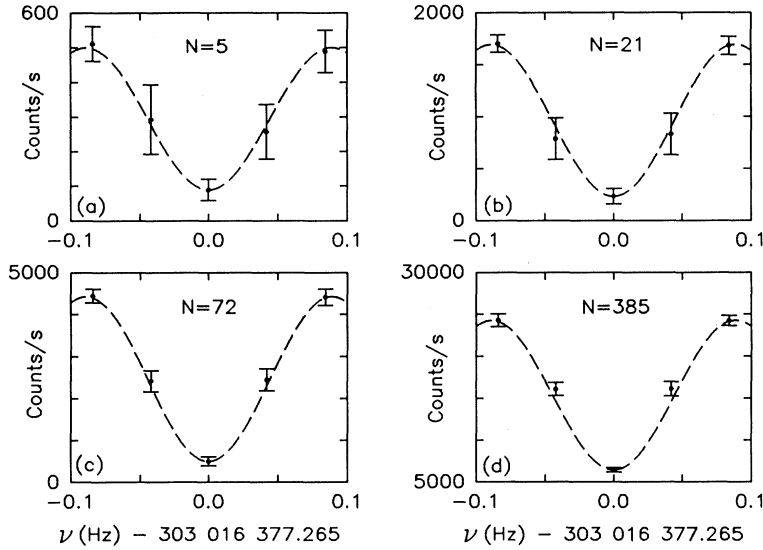
FIG. 11. Plots of the fluorescence detected from $^9\mathrm{Be}^+$ ions confined in a Penning trap as a function of the frequency of the applied rf radiation for (a) 5 ions, (b) 21 ions, (c) 72 ions, and (d) 385 ions. The dots are the experimental mean signals, and the error bars show the experimental standard deviations. On the sides of the resonances, the standard deviations are mainly due to quantum projection noise. The dashed lines show the calculated line shapes, fitted to the experimental minimum and maxima.

73.9, 58.0, and 48.6 counts/ion, respectively. The fact that $K \gg 1$ for all of these cases means that quantum projection noise should be more important than photon shot noise, except when the vanishing of one of the state amplitudes causes the quantum projection noise to go to zero. This is a good example of electron-shelving detection. In Figs. 11(a)–11(d), the dots are the experimental mean signals:

$$\overline{S} \equiv \frac{1}{n} \sum_{i=1}^{n} S_i, \tag{4.2}$$

where $S_1, S_2, \ldots, S_n$ is the sequence of n measurements made under the same conditions. The error bars correspond to $\pm\sigma$, where σ was calculated from

$$\sigma^2 = \frac{1}{2(n-1)} \sum_{i=1}^{n-1} (S_{i+1} - S_i)^2. \tag{4.3}$$

Equation (4.3) was used, rather than the usual formula,

$$\sigma^2 = \frac{1}{n-1} \sum_{i=1}^{n} (S_i - \overline{S})^2, \tag{4.4}$$

for the standard deviation, because it is less sensitive to slow drifts of the signal, such as those caused by variations in the laser intensity or other experimental parameters [41].

Table I summarizes the data shown graphically in Figs. 11(a)–11(d). For each value of N, the data from the point of minimum fluorescence is labeled "dip," the data from the two points of maximum fluorescence are combined and labeled "peaks," and the data from the two points halfway between the minimum and the maxima are combined and labeled "sides."

Four contributions to σ^2 are listed in Table I: σ^2_{proj},

σ^2_{pump}, σ^2_{shot}, and σ^2_{tech}. They are assumed to be independent, so they are added in quadrature to yield σ^2_{calc}:

$$\sigma^2_{\mathrm{calc}} \equiv \sigma^2_{\mathrm{proj}} + \sigma^2_{\mathrm{pump}} + \sigma^2_{\mathrm{shot}} + \sigma^2_{\mathrm{tech}}. \tag{4.5}$$

The quantum projection noise σ_{proj} is approximately zero at the peaks and at the dip and is $\frac{1}{2}(\frac{16}{17}N)^{1/2}K$ on the sides [see Eq. (2.41)]. The factor of $\frac{16}{17}$ appears in this expression because, on the average, $\frac{1}{17}$ of the ions are left in state 5 by the optical pumping that precedes the rf pulses. The fluctuations in the number of ions left in state 5 are the source of σ_{pump}. This has the greatest effect at the dip, where the only contribution to the fluorescence is from the ions in state 5. At the dip,

$$\sigma_{\mathrm{pump}} = \left[N(\tfrac{1}{17})(\tfrac{16}{17})\right]^{1/2} K = \tfrac{4}{17}\sqrt{N}K. \tag{4.6}$$

This is derived from the expression for the variance of a binomial distribution [see Eq. (2.18)]. At the peaks, σ_{pump} is approximately zero, because all of the ions are either in state 4 or state 5 and contribute to the signal. At the sides, σ_{pump} is half as large as at the dip. The shot noise σ_{shot} is equal to $(\overline{S})^{1/2}$ and results from Poisson statistics in the photon detection.

All other contributions to σ, such as those due to intensity fluctuations of the laser, are called technical noise σ_{tech}. Laser-intensity fluctuations will lead to a contribution to σ_{tech} proportional to S. Fluctuations in the shape and temperature of the ion plasma may make a large contribution to σ_{tech}, approximately proportional to S. Such fluctuations have been observed in other laser-cooled ion plasmas in Penning traps [42,43], but are not well understood. Small fluctuations in the frequency of the microwave source, or in the resonance frequency of the ions, would cause an increase in σ_{tech} on the sides of the line shape but not at the dips or peaks. However, from auxiliary measurements, including the observation

TABLE I. Mean signals $\overline{S}$ and variances σ^2 for $N = 5$, 21, 72, and 385 $^9\text{Be}^+$ ions. The terms "dip," "peaks," and "sides" refer to the points of minimum fluorescence, the points of maximum fluorescence, and the points halfway between the minima and the maxima, respectively. The number of measurements is n. The measured variance is σ^2_{expt}. The calculated variance σ^2_{calc} is equal to $\sigma^2_{\text{proj}} + \sigma^2_{\text{pump}} + \sigma^2_{\text{shot}} + \sigma^2_{\text{tech}}$. The value of σ^2_{expt} at the peaks was used to empirically determine σ^2_{tech}. Hence σ^2_{calc} is not listed at the peaks, since it is necessarily equal to σ^2_{expt}. However, the agreement between σ_{expt} and σ_{calc} at the sides and at the dip is a test of the theory. The units for the variances are 10^3 counts^2.

N	Position	n	$\overline{S}$ (counts)	σ^2_{expt}	σ^2_{proj}	σ^2_{pump} (10^3 counts^2)	σ^2_{shot}	σ^2_{tech}	σ^2_{calc}
5	dip	19	89	1.0	≈ 0	2.1	0.1	0.1	2.3
5	sides	38	275	6.6	9.0	0.5	0.3	0.7	10.5
5	peaks	38	500	2.8	≈ 0	≈ 0	0.5	2.3	
21	dip	30	232	5.5	≈ 0	6.3	0.2	0.1	6.6
21	sides	60	810	37.8	27.0	1.6	0.8	1.3	30.7
21	peaks	60	1 693	7.6	≈ 0	≈ 0	1.7	5.9	
72	dip	30	498	11.5	≈ 0	13.4	0.5	0.3	14.2
72	sides	60	2 432	61.0	57.0	3.4	2.4	6.3	69.1
72	peaks	60	4 429	25.2	≈ 0	≈ 0	4.4	20.8	
385	dip	30	6 642	69	≈ 0	50	7	26	83
385	sides	60	16 108	600	214	13	16	151	394
385	peaks	60	24 253	367	≈ 0	≈ 0	24	343	

of lineshapes as narrow as 900 μHz [34], we determined that this potential source of noise was negligible. Since known contributions to σ_{tech} are roughly proportional to S, σ_{tech} was determined empirically from σ_{expt} at the peaks, where the only other contribution to σ is σ_{shot}, which is small. For $N = 5$, 21, 72, and 385, $\sigma_{\text{tech}}/\overline{S}$ at the peaks was 9.6%, 4.5%, 3.2%, and 2.4%, respectively. The values of σ_{tech} at the sides and the dips were estimated by assuming that, for a given set of experimental conditions, σ_{tech} was proportional to $\overline{S}$.

The entries on Table I show that different types of noise dominate at each of the three positions on the line: σ^2_{proj} on the sides, σ^2_{pump} at the dip, and σ^2_{tech} at the peaks. Shot noise is not a large contribution for any of the cases shown in Table I. Considering the uncertainties in the experimental parameters, particularly in N, the agreement between σ^2_{expt} and σ^2_{calc} is quite good. Figure 12 shows that the noise on the sides of the lines is mainly attributable to quantum projection noise. The quantity plotted is $\sigma/\Delta S$ and is defined as

$$\frac{\sigma}{\Delta S} \equiv \frac{\sigma_{\text{expt}}(\text{sides})}{\overline{S}(\text{peaks}) - \overline{S}(\text{dip})}. \qquad (4.7)$$

The dashed line is the theoretical prediction for quantum projection noise alone:

$$\frac{\sigma_{\text{proj}}}{\Delta S} = \frac{\sqrt{17}}{8\sqrt{N}} \approx \frac{0.515}{\sqrt{N}}. \qquad (4.8)$$

The deviation of the experiment from theory for large N is presumably due to technical noise. As noted previously, $\sigma_{\text{tech}}/\overline{S}$ decreases as N increases, apparently because the ion plasma becomes more stable in shape and

temperature. However, it should not continue to decrease indefinitely with N, since the contribution from laser intensity fluctuations, for example, should approach a constant value for large N. Hence $\sigma/\Delta S$ should approach a constant value for large N rather than continuing to decrease as $1/\sqrt{N}$. For $N = 10\,000$, $\sigma_{\text{proj}}/\overline{S}$ is approximately 1% on the sides, while we might, from the present results, expect $\sigma_{\text{tech}}/\overline{S}$ to be about 2%. This is consistent with previous experimental results from a frequency
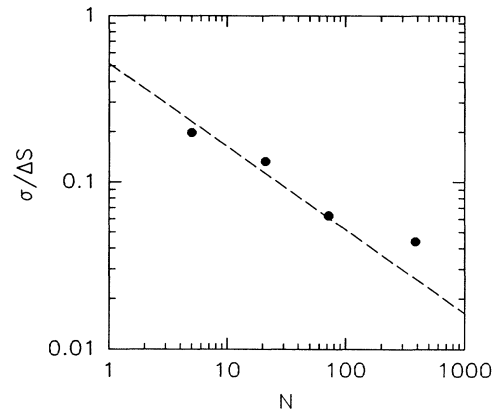

FIG. 12. Plot of the normalized standard deviations as a function of N, the number of $^9\text{Be}^+$ ions. The quantity $\sigma/\Delta S$ is the ratio of the experimental standard deviation on the sides of the resonance to the difference in the signal between the peaks and the dip. The dashed line is the theoretical prediction for the contribution from quantum projection noise alone.

standard based on 5000–10 000 $^9\text{Be}^+$ ions [34]. However, there is no fundamental reason that the technical noise cannot be greatly reduced.

V. CONCLUSION

We have prepared one or many ions in well-defined superpositions of two states and then measured the population of one of these states. The population measurements display quantum fluctuations which are greatest when the amplitudes of the two states are equal. In the case of a single ion, where photon scattering is used to distinguish between the two states, the fluctuations take the form of random switching between two distinguishable conditions — the observation of zero photons (or background) or of some photons. There is good agreement between the observations and theoretical predictions for both one and many ions.

Population fluctuations of the type observed here (quantum projection noise) are present and could be observed in other kinds of experiments, for example, those using atomic or neutron beams. Quantum projection noise might be observed in neutron interferometry [44]. In this case, the two neutron beams which emerge from the interferometer correspond to the two energy states $|A\rangle$ and $|B\rangle$. Introducing a phase shift in one arm of the interferometer allows one to create coherent superposition states. Rauch *et al.* [44] show counting-rate histograms for phase shifts corresponding to the maximum and minimum counting rates in one beam. However, they do not show the histograms for a phase shift halfway between a maximum and a minimum, which might show an increased variance due to quantum projection noise.

In the preceding discussions, the single-atom and N-atom experiments were treated from different perspectives. This was because of the different experimental methods which were used for the $^{199}\text{Hg}^+$ and $^9\text{Be}^+$. How-

ever, if the N atoms are uncorrelated, there is not a fundamental difference between the two cases. We could simulate the results of an N-atom measurement by making N successive measurements on a single atom and summing the results.

In many experiments, quantum projection noise would be obscured by other forms of noise, such as fluctuations in the beam intensity or the statistics of the detection process. In the experiments described here, trapping nearly eliminates fluctuations in the number of atoms, and the electron-shelving detection method nearly eliminates statistical fluctuations in the detection, thereby making quantum projection noise the dominant source of noise. In spectroscopic measurements on fixed numbers of atoms, where transitions are detected by monitoring changes in population, this is the fundamental noise limit.

ACKNOWLEDGMENTS

APPENDIX: OPTICAL PUMPING IN $^{199}\text{Hg}^+$

For low enough laser intensities, optical pumping among the Zeeman hyperfine sublevels of the ground state of $^{199}\text{Hg}^+$ can be described by population rate equations. The following set of equations applies to the populations of the Zeeman hyperfine sublevels of the $6s\,^2S_{1/2}$ and $6p\,^2P_{1/2}$ states, when a linearly polarized optical field of the form $\mathbf{E}(\mathbf{r},t) = \hat{\epsilon}E_0\cos(\mathbf{k}\cdot\mathbf{r} - \omega_k t)$, nearly resonant with the $^2S_{1/2}(F=1) \rightarrow {}^2P_{1/2}(F=0)$ transition, is applied:

$$\frac{dP_0}{dt} = -\left(\frac{\gamma/2}{\Delta_S + \Delta_P}\right)^2 R_0 P_0 + \frac{\gamma}{3}(P_5 + P_6 + P_7), \tag{A1}$$

$$\frac{dP_1}{dt} = -\tfrac{1}{2}\sin^2\theta\, R_0 L(\Delta) P_1 - \tfrac{1}{2}(1 + \cos^2\theta)\left(\frac{\gamma/2}{\Delta_P}\right)^2 R_0 P_1 + \frac{\gamma}{3}(P_4 + P_5 + P_6), \tag{A2}$$

$$\frac{dP_2}{dt} = -\cos^2\theta\, R_0 L(\Delta) P_2 - \sin^2\theta\left(\frac{\gamma/2}{\Delta_P}\right)^2 R_0 P_2 + \frac{\gamma}{3}(P_4 + P_5 + P_7), \tag{A3}$$

$$\frac{dP_3}{dt} = -\tfrac{1}{2}\sin^2\theta\, R_0 L(\Delta) P_3 - \tfrac{1}{2}(1 + \cos^2\theta)\left(\frac{\gamma/2}{\Delta_P}\right)^2 R_0 P_3 + \frac{\gamma}{3}(P_4 + P_6 + P_7), \tag{A4}$$

$$\frac{dP_4}{dt} = \tfrac{1}{2}\sin^2\theta\, R_0 L(\Delta)(P_1 + P_3) + \cos^2\theta\, R_0 L(\Delta) P_2 - \gamma P_4, \tag{A5}$$

$$\frac{dP_5}{dt} = \tfrac{1}{2}\sin^2\theta\left(\frac{\gamma/2}{\Delta_S + \Delta_P}\right)^2 R_0 P_0 + \cos^2\theta\left(\frac{\gamma/2}{\Delta_P}\right)^2 R_0 P_1 + \tfrac{1}{2}\sin^2\theta\left(\frac{\gamma/2}{\Delta_P}\right)^2 R_0 P_2 - \gamma P_5, \tag{A6}$$

$$\frac{dP_6}{dt} = \cos^2\theta\left(\frac{\gamma/2}{\Delta_S + \Delta_P}\right)^2 R_0 P_0 + \tfrac{1}{2}\sin^2\theta\left(\frac{\gamma/2}{\Delta_P}\right)^2 R_0(P_1 + P_3) - \gamma P_6, \tag{A7}$$

$$\frac{dP_7}{dt} = \tfrac{1}{2}\sin^2\theta\left(\frac{\gamma/2}{\Delta_S + \Delta_P}\right)^2 R_0 P_0 + \tfrac{1}{2}\sin^2\theta\left(\frac{\gamma/2}{\Delta_P}\right)^2 R_0 P_2 + \cos^2\theta\left(\frac{\gamma/2}{\Delta_P}\right)^2 R_0 P_3 - \gamma P_7. \tag{A8}$$

Figure 13 shows the correspondence between the numerical state labels used in Eqs. (A1)–(A8) and the quantum numbers. The labels 0–3 correspond to the $6s\,^2S_{1/2}$ $(F = 0, M_F = 0)$, $(F = 1, M_F = -1)$, $(F = 1, M_F = 0)$, and $(F = 1, M_F = 1)$ states, respectively. The labels 4–7 correspond to the $6p\,^2P_{1/2}(F = 0, M_F = 0)$, $(F = 1, M_F = -1)$, $(F = 1, M_F = 0)$, and $(F = 1, M_F = 1)$ states, respectively. The quantity γ is the natural decay rate of the $^2P_{1/2}$ state, $\hbar\Delta_S$ and $\hbar\Delta_P$ are the $^2S_{1/2}$ and $^2P_{1/2}$ hyperfine energy splittings, and θ is the angle between the z axis, defined by the magnetic field, and $\hat{\epsilon}$. The quantity R_0, which has dimensions of inverse time, is

$$R_0 \equiv \frac{|E_0(6p\,^2P_{1/2} \parallel D^{(1)} \parallel 6s\,^2S_{1/2})|^2}{6\gamma\hbar^2}, \qquad (A9)$$

where $(6p\,^2P_{1/2} \parallel D^{(1)} \parallel 6s\,^2S_{1/2})$ is a reduced matrix element of the electric-dipole-moment operator, defined according to the conventions of Edmonds [19]. The quantity $L(\Delta)$ is a Lorentzian resonance line shape, defined by

$$L(\Delta) \equiv \frac{(\gamma/2)^2}{\Delta^2 + (\gamma/2)^2}, \qquad (A10)$$

where $\Delta \equiv \omega_k - \omega_0$ is the laser detuning from the $^2S_{1/2}(F = 1) \rightarrow \,^2P_{1/2}(F = 0)$ resonance frequency ω_0. We consider the low-intensity limit, defined by $R_0 L(\Delta) \ll \gamma$. A typical experimental value for $R_0 L(\Delta)$ was 10^7 s^{-1}, while γ is 4.3×10^8 s^{-1}. The Zeeman shifts are not included in Δ, because they are assumed to be small compared to γ. For a typical magnetic field of 5×10^{-4} T, states 1 and 3 are separated from state 2 by $\pm$ 7 MHz, while γ, in the same units, is 70 MHz.

When a second laser near the $^2S_{1/2}(F = 0) \rightarrow \,^2P_{1/2}(F = 1)$ resonance is present, the atom spends nearly all of its time in the $^2S_{1/2}(F = 1)$ and $^2P_{1/2}(F = 0)$ states. The following reduced set of rate equations then describes the system:

$$\frac{dP_1}{dt} = -\tfrac{1}{2}(\sin^2\theta)R_0 L(\Delta)P_1 + \tfrac{1}{3}\gamma P_4, \qquad (A11)$$

$$\frac{dP_2}{dt} = -(\cos^2\theta)R_0 L(\Delta)P_2 + \tfrac{1}{3}\gamma P_4, \qquad (A12)$$

$$\frac{dP_3}{dt} = -\tfrac{1}{2}(\sin^2\theta)R_0 L(\Delta)P_3 + \tfrac{1}{3}\gamma P_4, \qquad (A13)$$

$$\frac{dP_4}{dt} = \tfrac{1}{2}(\sin^2\theta)R_0 L(\Delta)(P_1 + P_3)$$
$$+ (\cos^2\theta)R_0 L(\Delta)P_2 - \gamma P_4. \qquad (A14)$$

The mean populations of the states are obtained by setting the time derivatives in Eqs. (A11)–(A14) to zero. The mean populations are

$$P_1 \approx \frac{2\cos^2\theta}{1 + 3\cos^2\theta}, \qquad (A15)$$

$$P_2 \approx \frac{\sin^2\theta}{1 + 3\cos^2\theta}, \qquad (A16)$$

$$P_3 \approx \frac{2\cos^2\theta}{1 + 3\cos^2\theta}, \qquad (A17)$$
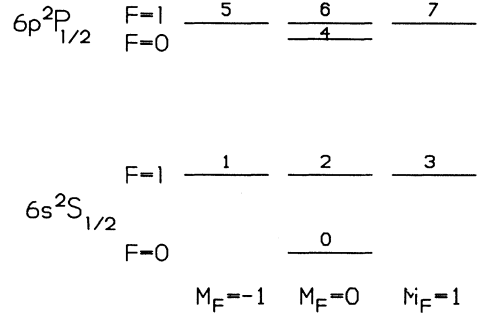

FIG. 13. Hyperfine Zeeman sublevels of the $6s\,^2S_{1/2}$ and $6p\,^2P_{1/2}$ states of ^{199}Hg$^+$. The labels 0–7 for the sublevels are used in the discussion of optical pumping in the Appendix.

$$P_4 \approx \frac{3\sin^2\theta\,\cos^2\theta}{1 + 3\cos^2\theta}\left[\frac{R_0 L(\Delta)}{\gamma}\right] \ll 1. \qquad (A18)$$

The dependence of P_4 on θ is of interest, because the number of fluorescence photons emitted per ion is γP_4. From Eqs. (A18)–(A15), it can be seen that the fluorescence goes to zero for $\theta = 0$ or π, when the population is pumped into states 1 and 2. The fluorescence also goes to zero for $\theta = \pi/2$, when the population is pumped into state 2. The fluorescence has its maximum value for $\cos\theta = 3^{-1/2}$ ($\theta \approx 54.7°$), when states 1, 2, and 3 are equally populated.

Another quantity of interest is the mean population of the $^2S_{1/2}(F = 1)$ state when only one laser beam is present. This quantity is equal to $P_1 + P_2 + P_3$ and can be determined from the steady-state solutions to Eqs. (A1)–(A8). In the low-intensity limit,

$$\frac{P_1 + P_2 + P_3}{P_0} \approx \left(\frac{\Delta_P}{\Delta_S + \Delta_P}\right)^2 \left[\frac{2(1 + 3\cos^2\theta)}{1 + 3\cos^4\theta}\right]. \qquad (A19)$$

The quantity inside the square brackets varies from 2 to 3, depending on θ. It reaches its maximum value for $\cos\theta = 3^{-1/2}$, the same value for which Eq. (A18) predicts the maximum fluorescence when both lasers are present. Since θ was set empirically so as to maximize the fluorescence, it was probably close to this value in the experiment. From Eq. (A19), and using $P_0 + P_1 + P_2 + P_3 \approx 1$, we find that $P_1 + P_2 + P_3$ lies between 0.041 and 0.06. This compares well with the experimental value of 0.053 ± 0.06 determined from the data shown in Fig. 7.

In order for the rate-equation approach to be valid, the laser intensity must not be too large. A density-matrix calculation including the coherences between states 1, 2, 3, and 4 shows that if the magnetic field is not large enough compared to the optical electric field, the atom is optically pumped into a nonfluorescing superposition state [45]. While the density-matrix approach is valid over a larger range of parameters, the rate-equation approach is used here because it is simpler and is still a good approximation for the low laser intensities which were used in the experiment.

* Present address: Department of Physics, University of Texas, Austin, TX 78712.

[1] L. E. Ballentine, Am. J. Phys. **55**, 785 (1987).

[2] L. E. Ballentine, Rev. Mod. Phys. **42**, 358 (1970).

[3] A. Peres, Am. J. Phys. **54**, 688 (1986).

[4] D. Home and M. A. B. Whitaker, Phys. Rep. **210**, 223 (1992).

[5] M. Pavičić, in *Problems in Quantum Physics II, Gdansk, 1989,* edited by J. Mizerski *et al.* (World Scientific, Singapore, 1990), pp. 440–452.

[6] D. Home and M. A. B. Whitaker, Phys. Lett. A **160**, 325 (1991).

[7] J. Dalibard, Y. Castin, and K. Mølmer, Phys. Rev. Lett. **68**, 580 (1992).

[8] H. J. Carmichael, R. J. Brecha, and P. R. Rice, Opt. Commun. **82**, 73 (1991).

[9] G. C. Hegerfeldt and T. S. Wilsner, in *Quantum Systems—Foundations and Symmetries: Proceedings of the Second International Wigner Symposium, Goslar, 1991,* edited by W. Scherer, H. D. Doebner, and F. Schroeck, Jr. (World Scientific, Singapore, 1992).

[10] R. Dum, P. Zoller, and H. Ritsch, Phys. Rev. A **45**, 4879 (1992).

[11] H. G. Dehmelt, Bull. Am. Phys. Soc. **20**, 60 (1975).

[12] D. J. Wineland, J. C. Bergquist, W. M. Itano, and R. E. Drullinger, Opt. Lett. **5**, 245 (1980).

[13] D. J. Wineland, W. M. Itano, J. C. Bergquist, and F. L. Walls, in *Proceedings of the 35th Annual Frequency Control Symposium, Philadelphia, 1981,* NTIS Doc. No. AD-A110870 (Electronic Industries Association, Washington, DC, 1981), pp. 602–611 [reprinted in *Trapped Ions and Laser Cooling,* edited by D. J. Wineland, W. M. Itano, J. C. Bergquist, and J. J. Bollinger, Natl. Bur. Stand. (U.S.) Technical Note 1086 (U.S. GPO, Washington, DC, 1985), pp. TN-47–TN-56].

[14] N. F. Ramsey, *Molecular Beams* (Oxford University Press, London, 1956).

[15] R. P. Feynman, F. L. Vernon, Jr., and R. W. Hellwarth, J. Appl. Phys. **28**, 49 (1957).

[16] R. H. Dicke, Phys. Rev. **93**, 99 (1954).

[17] P. R. Bevington, *Data Reduction and Error Analysis for the Physical Sciences* (McGraw-Hill, New York, 1969).

[18] F. T. Arecchi, E. Courten, R. Gilmore, and H. Thomas, Phys. Rev. A **6**, 2211 (1972).

[19] A. R. Edmonds, *Angular Momentum in Quantum Mechanics* (Princeton University Press, Princeton, NJ, 1974).

[20] B. Yurke, Phys. Rev. Lett. **56**, 1515 (1986); B. Yurke, S. L. McCall, and J. R. Klauder, Phys. Rev. A **33**, 4033 (1986).

[21] M. Kitagawa and M. Ueda, Phys. Rev. Lett. **67**, 1852 (1991); in *Noise in Physical Systems and 1/f Fluctuations,* Proceedings of the International Conference, Kyoto, Japan, 1991, edited by T. Musha, S. Sato, and M. Yamamoto (IOS, Burke, VA, 1992), p. 355.

[22] G. S. Agarwal and R. R. Puri, Phys. Rev. A **41**, 3782 (1990).

[23] D. J. Wineland, J. J. Bollinger, W. M. Itano, F. L. Moore, and D. J. Heinzen, Phys. Rev. A **46**, 6797 (1992).

[24] L. S. Cutler, R. P. Giffard, and M. D. McGuire, in *Proceedings of the 13th Annual Precise Time and Time Interval Applications and Planning Meeting,* edited by L. J. Rueger, NASA Conf. Publ. 2220 (NASA, Washington, DC, 1982), pp. 563–578.

[25] Y. Guern, A. Bideau-Méhu, R. Abjean, and A. Johannin-Gilles, Phys. Scr. **14**, 273 (1977).

[26] P. Eriksen and O. Poulsen, J. Quant. Spectrosc. Radiat. Transfer **23**, 599 (1980).

[27] W. M. Itano, J. C. Bergquist, R. G. Hulet, and D. J. Wineland, Phys. Rev. Lett. **59**, 2732 (1987).

[28] M. G. Raizen, J. M. Gilligan, J. C. Bergquist, W. M. Itano, and D. J. Wineland, J. Mod. Opt. **39**, 233 (1992); Phys. Rev. A **45**, 6493 (1992).

[29] H. Hemmati, J. C. Bergquist, and W. M. Itano, Opt. Lett. **8**, 73 (1983).

[30] See, for example, W. M. Itano and D. J. Wineland, Phys. Rev. A **25**, 35 (1982); D. J. Wineland and W. M. Itano, Phys. Today **40** (6), 34 (1987).

[31] A. G. Calamai and C. E. Johnson, Phys. Rev. A **42**, 5425 (1990).

[32] J. J. Bollinger, D. J. Heinzen, W. M. Itano, S. L. Gilbert, and D. J. Wineland, Phys. Rev. Lett. **63**, 1031 (1989).

[33] S. L. Gilbert, J. J. Bollinger, and D. J. Wineland, Phys. Rev. Lett. **60**, 2022 (1988).

[34] J. J. Bollinger, D. J. Heinzen, W. M. Itano, S. L. Gilbert, and D. J. Wineland, IEEE Trans. Instrum. Meas. **40**, 126 (1991).

[35] W. M. Itano, D. J. Heinzen, J. J. Bollinger, and D. J. Wineland, Phys. Rev. A **41**, 2295 (1990).

[36] D. J. Larson, J. C. Bergquist, J. J. Bollinger, W. M. Itano, and D. J. Wineland, Phys. Rev. Lett. **57**, 70 (1986).

[37] D. J. Wineland, J. J. Bollinger, W. M. Itano, and J. D. Prestage, J. Opt. Soc. Am. B **2**, 1721 (1985).

[38] L. R. Brewer, J. D. Prestage, J. J. Bollinger, W. M. Itano, D. J. Larson, and D. J. Wineland, Phys. Rev. A **38**, 859 (1988).

[39] R. G. Hulet and D. J. Wineland, Phys. Rev. A **36**, 2758 (1987).

[40] R. G. Hulet, D. J. Wineland, J. C. Bergquist, and W. M. Itano, Phys. Rev. A **37**, 4544 (1988).

[41] H. Mark and J. Workman, *Statistics in Spectroscopy* (Academic, San Diego, 1991), pp. 57–68.

[42] R. C. Thompson, G. P. Barwood, and P. Gill, Appl. Phys. B **46**, 87 (1988).

[43] W. M. Itano, L. R. Brewer, D. J. Larson, J. J. Bollinger, S. L. Gilbert, and D. J. Wineland, in *Frequency Standards and Metrology,* Proceedings of the Fourth Symposium, Ancona, Italy, edited by A. De Marchi (Springer-Verlag, Berlin, 1989), p. 447.

[44] H. Rauch, J. Summhammer, M. Zawisky, and E. Jericha, Phys. Rev. A **42**, 3726 (1990).

[45] W. M. Itano (unpublished calculations).